applied sciences

MDPI

Article

Silica-Coated Magnetic Nanocomposites for Pb^{2+} Removal from Aqueous Solution

Roxana Nicola [1], Otilia Costişor [1], Mihaela Ciopec [2], Adina Negrea [2], Radu Lazău [2], Cătălin Ianăşi [1], Elena-Mirela Picioruş [1], Adél Len [3], László Almásy [3], Elisabeta I. Szerb [1,*] and Ana-Maria Putz [1]

1 "Coriolan Dragulescu" Institute of Chemistry, Romanian Academy, 24 Mihai Viteazu Bvd., 300223 Timisoara, Romania; rcrisan@acad-icht.tm.edu.ro (R.N.); ocostisor@acad-icht.tm.edu.ro (O.C.); ianasic@acad-icht.tm.edu.ro (C.I.); epiciorus@acad-icht.tm.edu.ro (E.-M.P.); putzanamaria@acad-icht.tm.edu.ro (A.-M.P.)

2 Faculty of Industrial Chemistry and Environmental Engineering, Politehnica University of Timisoara, 6 Vasile Parvan Bvd., 300223 Timisoara, Romania; mihaela.ciopec@upt.ro (M.C.); adina.negrea@upt.ro (A.N.); radulazau@gmail.com (R.L.)

3 Centre for Energy Research, Konkoly-Thege 29-33, 1121 Budapest, Hungary; len.adel@energia.mta.hu (A.L.); almasy.laszlo@energia.mta.hu (L.A.)

* Correspondence: eszerb@acad-icht.tm.edu.ro or szella73@gmail.com

Received: 10 March 2020; Accepted: 10 April 2020; Published: 15 April 2020

Abstract: Magnetic iron oxide-silica shell nanocomposites with different iron oxide/silica ratio were synthesized and structurally characterized by Fourier transform infrared (FT-IR) spectroscopy, X-ray diffraction (XRD), small-angle neutron scattering, magnetic and N_2-sorption studies. The composite that resulted with the best properties in terms of contact surface area and saturation of magnetization was selected for Pb^{2+} adsorption studies from aqueous media. The material presented good absorption capacity (maximum adsorption capacity 14.9 $mg \cdot g^{-1}$) comparable with similar materials presented in literature. Its chemico-physical stability and adsorption capacity recommend the nanocomposite as a cheap adsorbent material for lead.

Keywords: magnetic nanoparticles; iron oxide-silica shell nanocomposite; lead adsorption

1. Introduction

The modernization of human life is directly linked with soil, air and water pollution, one of the main concerns being related to the development of industries that release into the environment untreated chemicals and toxic wastes. The removal of pollutants represents nowadays a global challenge and, in particular, heavy metals dispersed in the ambient are highly detrimental for human health being one of the major cause of cancer, birth defects or neurological problems to name a few, not to mention damage to flora and fauna [1]. Materials scientists have developed several strategies for the removal of heavy metals from water, ranging from chemical to physical, magnetic or electric techniques and the best performing in terms of cost, efficiency, simplicity, separation and regeneration seem to rely on chemical or physical adsorption [2]. Therefore different engineered nanomaterials were developed recently, including silica or carbon-based, metal or graphene oxide nanoparticles.

Among these, magnetic iron oxide nanoparticles emerged not only for their good adsorption properties, but also for the possibility of easy removal from aqueous systems [3]. Iron oxide magnetic nanoparticles (MNPs), indeed, were shown to have large surface areas with many active sites for adsorption of metal ions, good selectivity and low toxicity [4–7]. However, due to their hydrophobic surfaces, aggregation occurs in aqueous media, which lowers the efficiency of adsorption [8]. Therefore,

coating with organic or inorganic shells with porous, amorphous or ordered structures was carried out by several groups [9,10].

In this area, silica-based materials are hydrophilic and also considered as excellent adsorbents, being biocompatible, chemically and physically stable and cheap [11], so the combination of the two materials is considered a winning strategy for obtaining the best absorbents. Moreover, silica coating due to the abundant presence of hydroxyl groups facilitates the functionalization of the shell [7]. A thorough bibliographic search showed that great efforts have already been carried out to obtain MNPs@SiO_2/R nanocomposites, where R is usually an organic or hybrid organic-silica coating offering N or O-donor sites to coordinate the heavy metal center. Thus absorbents for heavy metals were obtained with Fe_3O_4@SiO_2/TSD-TEOS (TSD—(trimethoxysilyl)propyl]ethylenediamine, TEOS—tetraethyl orthosilicate) [12], Fe_3O_4@SiO_2/TETA (TETA—triethylenetetramine) [13], Fe_3O_4@SiO_2/Chitosan [14], Fe_3O_4@SiO_2/NH_2 [15], Fe_3O_4@SiO_2/Vaniline [16], Fe_3O_4@SiO_2/DMSA (DMSA—meso-2,3-dimercaptosuccinic acid) [17], MNPs@SiO_2/Bismuthiol II [18]. The synthesis usually involves a three-step procedure: (i) the obtaining of magnetic MNPs; (ii) the synthesis of MNPs@SiO_2 by the coating of MNPs with silica and (iii) a subsequent covering of the silica coating of MNPs@SiO_2 by co-condensation of another functional silica shell [19,20], covalent binding a functional derivative [12] or adsorption through electrostatic attraction between opposite charges [14].

Surprisingly, no systematic studies have been reported on the adsorption properties of non-functionalized MNPs and MNPs@SiO_2 nanocomposites, although some groups investigated their abilities to adsorb heavy metals mostly comparative to the functionalized materials in order to highlight the improvement of their properties post-functionalization [13,15–17] and there is one report on core-shell Fe_3O_4@SiO_2 microspheres showing Pb^{2+} removal efficiencies of 97% and good recyclability [21]. Both Fe_3O_4 nanoparticles and Fe_3O_4@SiO_2 nanocomposites are good adsorbents especially for Pb^{2+} ions due to the quite strong non-covalent interactions between the metal ion stereochemically active lone pair of electrons and the octahedral voids of Fe_3O_4 in the former and electrostatic interactions between the positively charged metal and negatively charged SiO_2 coating in the latter [14]. The adsorptive properties of the iron oxide-silica shell nanocomposites depend on their morphology on the one hand and conditions of determination (pH, contact time, temperature, initial concentration of Pb^{2+} in solution, eventual interference) on the other.

Based on this background, herein we report the synthesis of MNPs@SiO_2 magnetic nanocomposites by using a two steps method and their adsorptive properties for Pb^{2+} ions from aqueous media. A different ratio between iron oxide nanoparticles and silica was used in the synthesis process of MNPs@SiO_2 in order to determine the best conditions for obtaining iron oxide-silica shell nanocomposites with high surface area and the adsorption of Pb^{2+} ions was determined for the probe with the highest surface and best saturation magnetization (Ms) values.

2. Materials and Methods

$FeSO_4 \cdot 7H_2O$ (SigmaAldrich >99.5%, extrapure), $FeCl_3 \cdot 6H_2O$ (Merck >99%, p.a.), NaOH (LACHEMA >98%, p.a.), tetraethyl ortosilicate (TEOS) (Merck >99%, for synthesis), absolute ethanol (Riedel-de Haen, 99.8% vol.), NH_3 (Silan Trading 25%) were used without further purification. The structure and phase composition of the particles was determined by X-ray diffraction (XRD), using an Ultima IV (RIGAKU) instrument operating with Cu K radiation. The mean crystallite size was calculated using the WPPF (whole-pattern profile fitting) method and the instrument influence was subtracted using the diffraction pattern of a Si standard recorded in the same conditions. Nitrogen desorption isotherms were determined at 77 K using a Nova 1200e (QUANTACHROME) device, pore size distributions were derived with the Barrett–Joyner–Halenda (BJH) method; specific surface areas were determined using the Brunauer–Emmett–Teller (BET) method. Prior analyses, the probes were degassed in vacuum for 5 h at room temperature. The surface area for various batches synthesized were repeated in the same conditions and the results indicate values within the standard error of 5%. The magnetic properties were investigated in 50 Hz alternating

current (ac) fields of amplitudes up to 6.4 kOe by means of a laboratory-manufactured induction hysteresigraph [22]. The instrument provides two voltage signals reproducing the time evolution of the applied field and sample contribution to the magnetic flux (at 3 Oe/V, and 0.1 Mx/V, respectively, calibration error), which were recorded at 150 kHz sampling frequency to a PC by means of a 16 bit-resolution DT-9816A (DATA TRANSLATION) data acquisition card. The saturation magnetization (technical) was estimated from extrapolating to 50 kOe the data resulted from fitting the hysteresis loop branches to a superposition of Langevin-type transition functions. [22]. The saturation magnetization was estimated from extrapolating to 50kOe the fitted data. Infrared spectra were collected in KBr in the range 4000–400 cm^{-1} on a Cary 630 Fourier transform infrared (FT-IR) spectrophotometer. Small-angle neutron scattering (SANS) measurements were performed at the *Yellow Submarine* spectrometer at the Budapest Neutron Centre, using standard instrument configurations and data processing. The samples were measured at ambient temperature. The data were fitted to analytical model equation introduced by Beaucage [23] using Igor Pro software.

2.1. Synthesis of Magnetic MNPs@SiO2 Nanocomposites

Separate batches of magnetic iron oxide nanoparticles were freshly obtained prior to each coating operation with various amounts of silica. MNPs were obtained by the alkaline reverse co-precipitation method using NaOH, following the synthetic strategy previously reported [24]. In particular, 43 mL $FeCl_3 \cdot 6H_2O$ (0.1 M) and 25 mL $FeSO_4 \cdot 7H_2O$ solutions (0.1 M) separately prepared were mixed and added to 25 mL NaOH solution (1 M). The reaction mixture was stirred (300 rpm) for 30 min at room temperature. After several washing steps with water and absolute ethanol, the black magnetic precipitate obtained was ready for the coating step with silica, carried out following an adapted Stöber method. In particular, a solution composed of TEOS, ethanol and water was obtained by mixing adequate quantities of TEOS and ethanol for 10 min at 300 rpm, and then water was added (see Table 1). The resulting solution was added to the prepared iron oxide nanoparticles (see Table 1) and mixed for 10 min at 300 rpm. The hydrolysis and condensation of TEOS was initiated by the addition of ammonia solution (25%) to the reaction mixture. The reaction occurred under constant stirring and at room temperature for 3 h, and was then aged for 10 days at room temperature. The precipitate obtained was washed with absolute ethanol to remove unreacted species and dried at 60 °C, in oven for 12 h.

Table 1. Summary of synthesis parameters.

Sample	TEOS (mL)	Ethanol (mL)	H_2O (mL)	NH_3 Solution 25% (mL)	TEOS: Ethanol: H_2O: NH_3 Molar Ratio	Targeted Iron Oxide Concentration (Mass %) in Silica Matrix
MNPs35@SiO_2	3.5	18.6	6.89	0.23	1:20:25:0.2	35
MNPs21@SiO_2	7	37.2	13.78	0.46	1:20:25:0.2	21
MNPs15@SiO_2	10.5	55.8	20.67	0.7	1:20:25:0.2	15

2.2. Determination of Point of Zero Charge (pZc)

Batch equilibration technique was used. In particular, samples of 0.1 g of the adsorbent were suspended in 25 mL solution of 0.1 M KCI and the value of initial pH (pH_i) was varied in the range of 1–10 using NaOH solution. Samples were kept in a Julabo SW23 thermostatic bath, for 1 h at 298 K and 200 rpm. Once the contact time has passed, the final pH (pH_f) was read using a SevenCompact S 210 Mettler Toledo pH meter.

2.3. Adsorption Capacity

All samples were kept in contact in a thermostatic bath (Julabo SW23) rotating at 200 rpm. The adsorbent was magnetically separated from the aqueous solution and the residual concentration of Pb^{2+} ions was determined by atomic absorption spectroscopy using a Varian AAS 280 FS atomic absorption spectrometer. Different concentration Pb^{2+} solutions were obtained by dilution from a stock solution of 1000 mg/L $Pb(NO_3)$ in nitric acid 0.5 mol/L Certipur® Standard, Merck.

2.3.1. Effect of the pH on the Adsorption Capacity

We suspended 0.1 g of the adsorbent in 25 mL solution of 10 mg·L^{-1} Pb^{2+} solution, for 1 h at 298 K. To adjust the pH of Pb^{2+} solutions in the 1–6 range, NaOH aqueous solution was used. Studies have not been conducted at pH > 6 because there is a risk of lead precipitation. The residual concentration was determined.

2.3.2. Effect of Contact Time and Temperature on the Adsorption Capacity

We added 0.1 g of sample to 25 mL of Pb^{2+} solutions of 10 mg L^{-1} concentration, for different contact times (30, 45, 60, 90, 120 and 180 min), in a thermostatic water bath at different temperatures (298 K, 308 K and 318 K).

2.3.3. Effect of Initial Metal Ion Concentration on the Adsorption Capacity

Different initial concentration of Pb^{2+} in solution (5, 7.5, 10, 20, 25, 30, 40, 50, 75, 100 and 120 mg L^{-1}) was obtained from a stock solution of 1000 mg L^{-1} Pb^{2+}. The amount of adsorbent was fixed at 0.1 g, contact time and temperature were 90 min and 289 K, respectively.

2.4. Modeling of Sorption Isotherms, Kinetics and Thermodynamics

In the adsorption process, dissolved Pb^{2+} ions are binding to the adsorbent surface through physical or physico-chemical interactions until the equilibrium is reached. The equilibrium adsorption capacity (q_e) was calculated using Equation (1):

$$q_e = \frac{(C_0 - C_e)V}{m} \quad (1)$$

where: q_e—equilibrium adsorption capacity (mg·g^{-1}); C_0—initial concentration of metal ions (mg·L^{-1}), C_e—equilibrium concentration of metal ions (mg·L^{-1}); V—volume of aqueous solution containing metal ions content (L); m—mass of adsorbent (g).

2.4.1. Adsorption Isotherms

Three models of equilibrium isotherms were used, namely: (i) Langmuir isotherm (Equation (2)), which is based on the monolayer adsorption of the solute; (ii) Freundlich isotherm (Equation (3)), which was originally developed for heterogeneous surfaces and (iii) Sips model, which is a model that combines the aforementioned models, Langmuir and Freundlich. The equilibrium isotherms were obtained by the graphical representation of the q_e function of C_e, and the related parameters were obtained for each isotherm. The Langmuir and Freundlich constants were calculated using the linearized form of the resulting patterns after fitting.

Langmuir isotherm:

$$q_e = \frac{q_L \cdot K_L \cdot C_e}{1 + K_L \cdot C_e} \quad (2)$$

where: q_L—Langmuir maximum adsorption capacity (mg·g^{-1}); K_L—Langmuir constant.

Freundlich isotherm:

$$q_e = K_F \cdot C_e^{1/n_f} \quad (3)$$

where: K_F and n_f—characteristic constants that can be associated with the relative adsorption capacity of the adsorbent and the adsorption intensity.

Sips isotherm:

$$q_e = \frac{q_s \cdot K_s \cdot C_e^{1/n_s}}{1 + K_s \cdot C_e^{1/n_s}} \quad (4)$$

where: q_S—maximum adsorption capacity ($mg \cdot g^{-1}$); K_S—constant related to adsorbent adsorption capacity; n_S—heterogeneity factor.

2.4.2. Adsorption Kinetics

The pseudo-first order kinetic models, or the Lagergren model (Equation (5)) and pseudo-second order, or the Ho and McKay model (Equation (6)) were applied to describe the kinetics of the adsorption of Pb^{2+} during the process. A linear plot of $\ln(q_e\text{-}q_t)$ function of time gives the equilibrium adsorption capacity, $q_{e,calc}$ as intercept and the slope gives the k_1 rate constant for the pseudo-first-order kinetic model; a linear plot of t/q_t function of time gives the slope as equilibrium adsorption capacity $q_{e,calc}$ and the intercept gives the k_2 rate constant for the pseudo-second-order kinetic model.

Kinetic model

$$\ln\left(q_e - q_t\right) = \ln q_e - k_1 t \tag{5}$$

where: q_t—adsorption capacity at time t ($mg \cdot g^{-1}$); k_1—pseudo-first order constant ($1 \cdot min^{-1}$); t—contact time (min).

Ho and McKay model

$$\frac{t}{q_t} = \frac{1}{k_2 q_e^2} + \frac{t}{q_e} \tag{6}$$

where: k_2—rate constant of pseudo-second order adsorption model ($g \cdot (mg \cdot min)^{-1}$).

2.4.3. Thermodynamics of the Adsorption Process

The thermodynamics offer general information about the influence of temperature on the adsorption and it is suitable to predict the feasibility of the adsorption process. To determine how the Pb^{2+} ions adsorption proceeds on the surface of the adsorbent, Gibbs' free energy ($\Delta G°$) was calculated using the Gibbs–Helmholtz equation (Equation (7)).

$$\Delta G° = \Delta H° - T \cdot \Delta S° \tag{7}$$

where: $\Delta G°$—standard variation of the Gibbs' free energy ($kJ \cdot mol^{-1}$); $\Delta H°$—standard variation of enthalpy ($kJ \cdot mol^{-1}$); $\Delta S°$—standard variation of entropy ($J \cdot (mol \cdot K)^{-1}$); T—absolute temperature (K).

The standard variation of entropy $\Delta S°$ and, respectively, enthalpy $\Delta H°$ were calculated from the slope and the intercept of the linear plot of $\ln K_d$ as a function of the 1/T (Equation (8)).

$$\ln K_d = \frac{\Delta S°}{R} - \frac{\Delta H°}{RT} \tag{8}$$

where: K_d—constant of equilibrium; $\Delta S°$—standard variation of entropy ($J \cdot (mol \cdot K)^{-1}$); $\Delta H°$—standard variation of enthalpy ($kJ \cdot mol^{-1}$); T—absolute temperature (K); R—ideal gas constant ($8.314\ J \cdot (mol \cdot K)^{-1}$).

The equilibrium constant is given by the ratio of the q_e and C_e (Equation (9)):

$$K_d = \frac{q_e}{C_e} \tag{9}$$

2.5. Desorption Studies

Desorption was performed by mixing 1g exhausted material containing adsorbed ions with 25 mL HCl 5%. The mixture was shaken for 4 h at 200 rpm at room temperature. After that the filtered adsorbent material was rinsed with distilled water and dried at 50 °C for 24 h. The material obtained can be reused in the adsorption process. In filtrate the concentration of Pb^{2+} was determined by atomic absorption spectrometry.

3. Results and Discussion

Average 10 nm diameter MNPs were obtained following a synthetic method previously reported [24]. To obtain an iron oxide-silica shell nanocomposite system with enhanced surface active area, the quantity of the TEOS used in the synthesis of $MNPs_4@SiO_2$ was varied. Indeed, it is known from literature that the morphology and the thickness of the coating are influenced considerably by the TEOS/iron oxide ratio [25]. Therefore, we synthesized three materials that differ by the content of the iron oxide, namely $MNPs35@SiO_2$, $MNPs21@SiO_2$ and $MNPs15@SiO_2$, where the number indicates the targeted mass percent of iron oxide in nanocomposites.

3.1. Structural Characterization of the Samples

3.1.1. X-Ray Diffraction (XRD) Studies

XRD patterns of the samples are presented in Figure 1, whereas in Table 2 mean crystallite size obtained by using the WPPF method are reported.

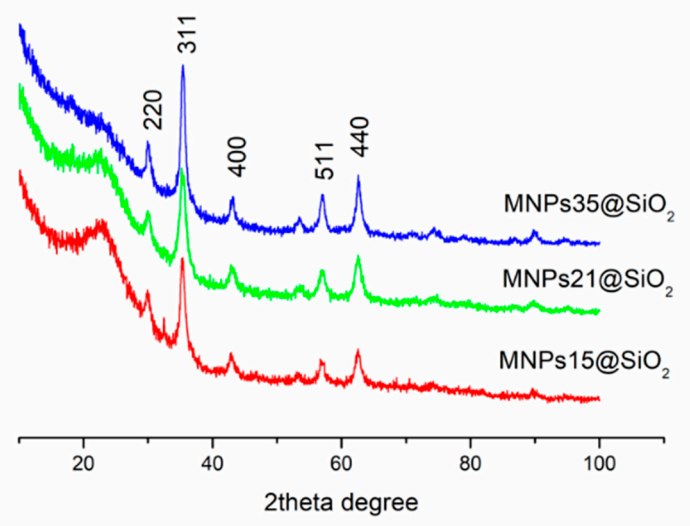

Figure 1. X-ray diffraction (XRD) patterns of the magnetic nanocomposites obtained.

Table 2. Average crystallite size.

Sample	Mean Crystallite Size (nm)
$MNPs35@SiO_2$	7.5 ± 0.3
$MNPs21@SiO_2$	6.3 ± 0.2
$MNPs15@SiO_2$	10.6 ± 0.4

The XRD diffraction patterns of the nanocomposites showed the characteristic peaks of cubic spinel structure (9009768 –COD Database). A visible wide diffraction peak at 2θ ~22–25° indicate the presence of amorphous silica. Taking into account that separate batches of magnetic iron oxide nanoparticles were freshly obtained prior to each coating operation with various amounts of silica, minor variations of the average crystallite size may be observed. However, these variations are in the range of 3 nm, which shows very good reproducibility and precise control of the co-precipitation process.

3.1.2. Fourier Transform Infrared (FT-IR) Spectroscopy

The FT-IR spectra of the nanocomposites are presented in Figure 2.

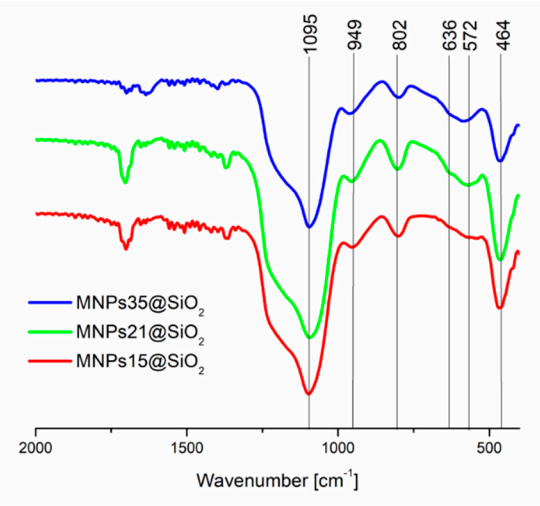

Figure 2. Fourier transform infrared (FT-IR) spectra of the magnetic nanocomposites.

The spectra indicate the presence of both iron oxide and silica in the composite materials, due to the identification of characteristic bands of both components: the typical stretching vibration of Fe–O [14] shifted to 570 cm^{-1} due to the Fe–O–Si bond formed, antisymmetric (1090 cm^{-1}) and symmetric (800 cm^{-1}) Si–O–Si stretching bands, Si–O–Si or O–Si–O bending (460 cm^{-1}) and Si–O stretching (950 cm^{-1}) [26].

3.1.3. Magnetic Measurements

In Figure 3 and Table 3 are presented the magnetization curves and magnetic parameters, respectively, of the synthesized nanocomposites.

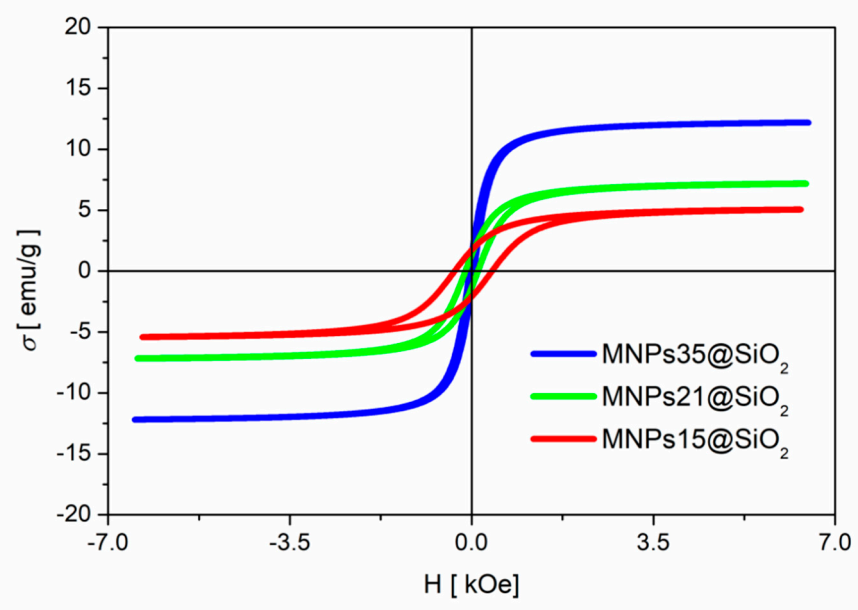

Figure 3. Magnetization curves of the magnetic nanocomposites.

Table 3. Magnetic parameters of nanocomposites.

Sample	Ms (emu/g)	Hc (Oe)	Mr (emu/g)
MNPs35@SiO_2	12.4	41.5	1.28
MNPs21@SiO_2	7.4	120	1.34
MNPs15@SiO_2	5.4	36	1.92

The saturation magnetization values are of the same order and the slight differences are caused by the variation of the silica coating thickness (content), since each sample contains a different amount of magnetic iron oxide, as per gram. The values of Ms, however, indicate a good response to an external magnetic field of the synthesized materials. This facilitates the separation of the material from the solution, an important feature in the application of this type of material as adsorbent for heavy metal ions from wastewater.

3.1.4. Small-Angle Neutron Scattering

Scattering at low angles allows one to obtain information on the structure of the materials on length scales 1–100 nm. The scattering curves of the investigated samples are presented in Figure 4 in logarithmic coordinates.

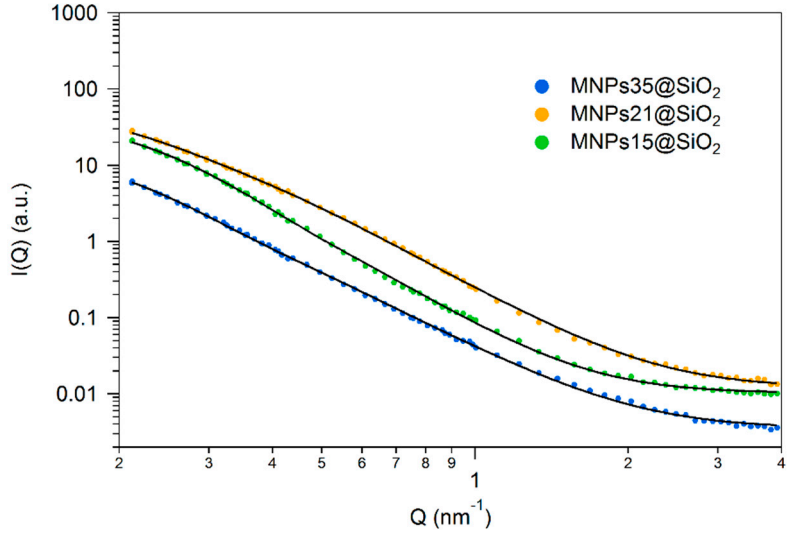

Figure 4. Small-angle neutron scattering (SANS) curves of the nanocomposites.

All data show a characteristic scattering pattern of materials having structural inhomogeneities on two characteristic sizes: the smaller sizes inhomogeneities—pores or particles produce a plateau or shoulder in the q range 0.3–0.8 nm^{-1} that corresponds to a size range of 5–30 nm, and a power law-like scattering that extends below the low q cut-off of the investigated q range, indicating a structural level larger than 200 nm. Fitting the data to the phenomenological Beaucage model [23] provides the size of the scattering entities collected in Table 4.

Table 4. Structural parameters of nanocomposites obtained by SANS.

Sample	Rg [nm]	p
MNPs35@SiO_2	10.1 ± 0.1	3.35 ± 0.01
MNPs21@SiO_2	9.1 ± 0.2	3.59 ± 0.01
MNPs15@SiO_2	8.8 ± 0.1	3.85 ± 0.01

In these composite materials, the average sizes of the embedded iron oxide particles (around 10 nm; XRD data and earlier studies [27]) and of the primary silica particles formed in the sol-gel process (5–10 nm [28,29]) are similar, therefore the applied model gives only an average size of these two structural components, that is the iron oxide particles and the primary silica particles. The monotonous increase of their average size or radius of gyration (Table 4) with an increasing amount of iron oxide shows that the synthesis method used permits to change continuously the textural properties of the materials. The fractal exponent P has typical values between 3 and 4, characteristic for rough interfaces

in silica xerogels [30,31]. The SANS results show that the nanocomposites have a complex irregular structure with agglomerate sizes above 200 nm, which is typical for air-dried silica xerogels.

3.1.5. N_2 Adsorption-Desorption Analysis

In Figure 5 are presented the nitrogen adsorption-desorption isotherms for the synthesized nanocomposites with the pore size distributions in the inset.

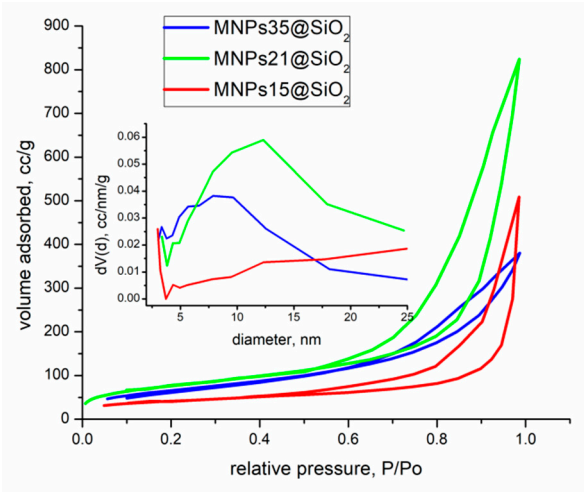

Figure 5. The N_2 adsorption-desorption isotherms of the magnetic nanocomposites. Inset: pore size distribution curves of the samples.

According to IUPAC classification [32], the adsorption-desorption isotherms of the samples correspond to a type IVa isotherm with a H3 hysteresis type. Type IV isotherm is typical for mesoporous materials, showing the characteristic hysteresis loop associated with the occurrence of pore condensation. The limiting uptake over a range of high P/P_0 results in a plateau on the isotherm, indicating complete pore filling. The initial part of the type IV isotherm is attributed to monolayer-multilayer adsorption. H_3 hysteresis is associated with non-rigid aggregates of plate-like particles which generate slit-like pores.

The specific surface area and total pore volume of nanocomposites increase with the increase of the targeted iron oxide concentration (Table 5) until a maximum of 270–275 m^2/g, reached for samples MNPs35@SiO_2 and MNPs21@SiO_2. All the synthesized nanocomposites presented large and disordered pore size distributions.

Table 5. Specific surface area, total pore volume and pore diameter of the samples.

Sample	Specific Surface Area [1] [m^2/g]	Total Pore Volume [cc/g]	Pore Diameter [2] [nm]
MNPs35@SiO_2	271	1.0	24.9
MNPs21@SiO_2	275	1.3	3.0
MNPs15@SiO_2	150	0.8	12.3

[1] calculated by MultiBET method [26]; [2] approximated from desorption branch using BJH (Barret–Joyner–Halenda) method.

To investigate the stability of MNPs35@SiO_2 nanocomposite in aqueous media N_2 adsorption-desorption isotherms before and after adsorption process of Pb^{2+} ions were carried out and the results are presented in Figure 6.

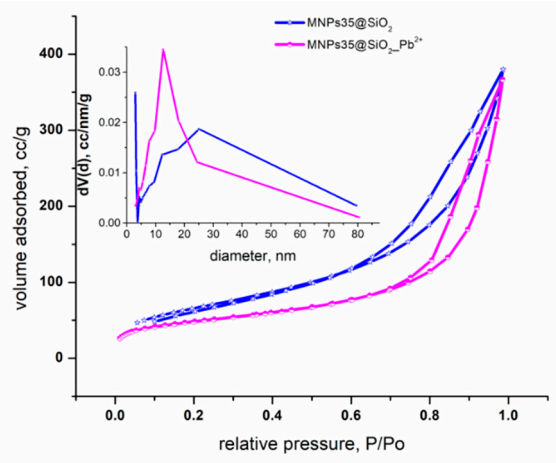

Figure 6. N_2 adsorption-desorption isotherms of the magnetic nanocomposite MNPs35@SiO_2 before and after Pb^{2+} ions adsorption

According to IUPAC classification, both adsorption-desorption isotherms, before and after Pb^{2+} ions adsorption, correspond to a type IVa isotherm with a H3 hysteresis. The structure of the nanocomposite has not changed after the adsorption process, indicating that the material has not degraded during the adsorption process. Specific surface area, total pore volume and pore diameter of the nanocomposite before and after the adsorption process are presented in Table 6.

Table 6. Specific surface area, total pore volume and pore diameter of MNPs35@AM_SiO_2 before and after Pb^{2+} ions adsorption.

Sample	Specific Surface Area [1] [m^2/g]	Total Pore Volume [cc/g]	Pore Diameter [2] [nm]
MNPs35@SiO_2	270.99	1.01	24.85
MNPs35@SiO_2_Pb(II)	174.38	0.57	12.64

[1] calculated by MultiBET method [26]; [2] approximated from desorption branch using BJH method.

From Table 6, it can be observed that the values of specific surface areas, total pore volume and pore diameter are decreasing after adsorption process of Pb^{2+} ions, indicating that a part of the pores are filled by the adsorbed Pb^{2+} ions.

3.2. Adsorption of Pb^{2+} Studies

Adsorption studies were carried out only for the sample presenting the highest surfaces and the best magnetic properties, which was the case of sample MNPs35@SiO_2. Prior to adsorption studies the point of zero charge of the sample was determined.

3.2.1. Point of Zero Charge (pZc)

The acid-base properties of the material play an important role in its use as an adsorbent. If the H^+/OH^- system are the potential determining ions, pZc is described in terms of pH value as the point of zero electrical charge. Determination of null electric point by batch equilibration techniques [33] for nanocomposite MNPs35@SiO_2 is presented in Figure 7.

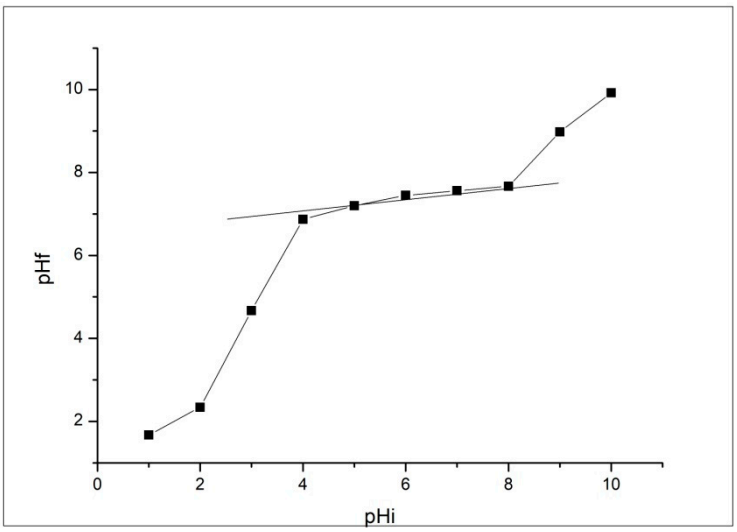

Figure 7. The pH_{PZC} of the magnetic nanocomposite MNPs35@SiO_2.

Figure 7 shows the appearance of the plateau of pH_{PZC} in the range of pH between 4–8. This means that the surface of the material, at pH values below 4, is predominantly positively charged and at values greater than 8, is predominantly negatively charged. In conclusion, for good efficiency of the adsorption process of the synthesised material, it is indicated that the pH of the solution with metal ions to be in the range of 4–8.

3.2.2. Effect of pH on the Adsorption of Pb^{2+} Ions

The pH value is an important factor in controlling the adsorption process performance of Pb^{2+} ions from aqueous solutions on the adsorbent [34] because its value influence not only the functional groups from the surface of the adsorbent, but also the chemical behaviour of the Pb^{2+} ions in aqueous solution. Indeed, hydrolysis, complexation of organic and/or inorganic ligands, redox reactions, precipitation of metal ions are pH-dependent and the pH strongly influence the speciation and adsorption availability [35,36]. Concentration of H^+ ions decreases with the increase of positive attraction forces between Pb^{2+} ions and free spaces from the surface of the negatively charged material, resulting in an increase of adsorption capacity. At low pH values, there is a strong competition between hydrogen ions and metal ions. A series of adsorption experiments were performed in aqueous medium at different pH values for the nanocomposite MNPs35@SiO_2 and the results obtained are shown in Figure 8.

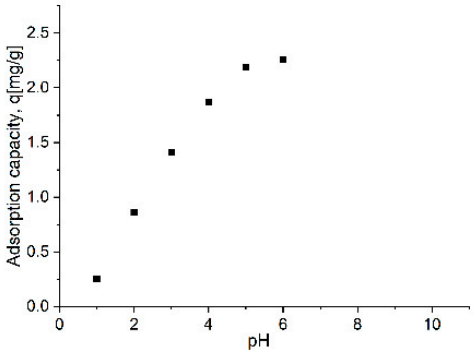

Figure 8. The effect of pH on the adsorption of Pb^{2+} ions on the magnetic nanocomposite MNPs35@SiO_2.

The increase of the pH up to 6 leads to the increase of the adsorption capacity until 2.25 $mg \cdot g^{-1}$. The optimum range of pH determined by pZc of adsorption of the nanocomposite MNPs35@SiO_2 is

4–6; however, at a pH > 6 lead can precipitate as $Pb(OH)_2$. Taking into account all factors is indicated to work at pH 4–6 [17,37]. As expected, the adsorption of Pb^{2+} ions is completely dependent on the pH: in acidic medium, the H^+ ions compete with the metal ions to reach the functional groups present on the surface of the nanocomposite, resulting a low adsorption capacity of Pb^{2+}, while with the increase of the pH the positively charged metal ions may be adsorbed at the negatively charged functional groups from the adsorbent surface due to the decrease of the competition between the H^+ ions and Pb^{2+} ions.

3.2.3. Effect of Contact Time and Temperature on the Adsorption of Pb^{2+} Ions

The plot of Pb^{2+} ions adsorption versus contact time with the nanocomposite MNPs35@SiO_2 at three temperatures (298, 308 and 318 K) is presented in Figure 9.

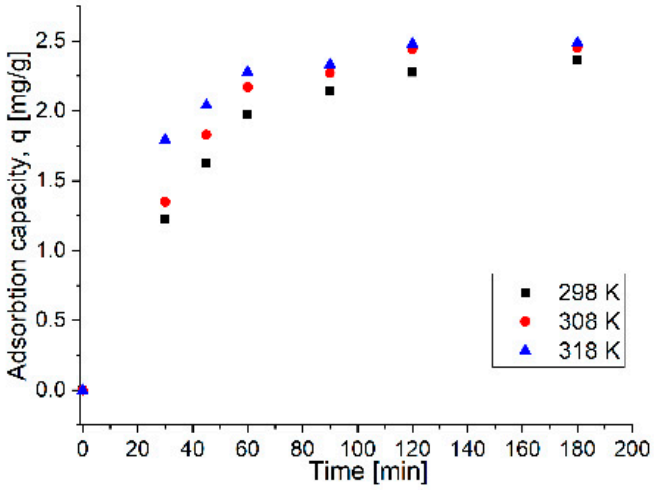

Figure 9. The effect of contact time and temperature for the Pb^{2+} adsorption on the magnetic nanocomposite MNPs35@SiO_2.

The experimental data shows that the adsorption capacity of the adsorbent material increases with contact time, reaching a maximum after 90 min. This high initial adsorption rate is due to the availability of a large number of adsorption sites present at the surface of the adsorbent at the beginning of the process. The selected contact time for further studies is set to 90 min. Increasing the temperature from 298 K to 318 K a small increase in the adsorption capacity, namely from 2.14 mg g^{-1} to 2.33 mg g^{-1} is obtained. This increase in adsorption capacity is economically insignificant, consequently the studies were continued at 298 K.

3.2.4. Adsorption Process Mechanism for Uptake the Pb^{2+} Ions onto the Magnetic Nanocomposite

Adsorption Kinetics

The kinetics of the Pb^{2+} adsorption process from aqueous solution using the nanocomposite MNPs35@SiO_2 are studied to show the efficiency of the adsorption process. The pseudo-first-order hand the pseudo-second-order kinetic equations were applied to explore the mechanisms of the adsorption processes. The fitting curves of $\ln(q_e\text{-}q_t)$ and t/q_t versus time are shown in Figure 10a,b, respectively. The relevant kinetic model parameters for Pb^{2+} adsorption are presented in Table 7.

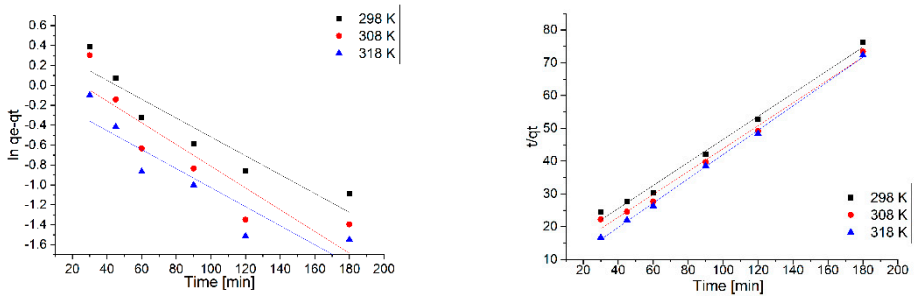

(**a**) (**b**)

Figure 10. Plots of pseudo- first- order (**a**) and pseudo- second- order (**b**) kinetic models for the Pb^{2+} adsorbtion onto magnetic nanocomposite MNPs35@SiO_2.

Table 7. Kinetic parameters of Pb^{2+} adsorption onto the magnetic nanocomposite.

Temperature [K]	Pseudo-First Order				Pseudo-Second Order			
	$q_{e,exp}$	k_1	$q_{e,calc}$	R^2	$q_{e,exp}$	k_2	$q_{e,calc}$	R^2
	(mg·g^{-1})	min^{-1}	(mg·g^{-1})		(mg·g^{-1})	(g·mg·min^{-1})	(mg·g^{-1})	
298	2.14	0.0095	1.55	0.8834	1.97	0.7044	2.84	0.9919
308	2.27	0.0109	1.32	0.8237	2.17	0.9195	2.86	0.9902
318	2.33	0.0095	1.07	0.8370	2.27	1.4628	2.69	0.9986

Kinetic models can identify the type of adsorption mechanism of the system and the potential stages to control the rate, including mass transport processes and chemical reactions [38]. The pseudo-first-order kinetic models, or the Lagergren model and pseudo-second-order, or the Ho and McKay model [39], were applied to describe the kinetics of the adsorption of Pb^{2+}. The kinetic model that describes best the adsorption process can be established based on the values of the resulting constants and the obtained regression coefficient (R^2). Thus, from the data presented in Table 7, it can be observed that the kinetic model of pseudo-second-order is the model that describe the adsorption process of Pb^{2+} ions on MNPs35@SiO_2 nanocomposite, since R^2 is in the range ~0.9919–0.9986, depending on temperature. This correlation is in line with the literature data showing that the adsorption process of Pb^{2+} ions is influenced by pH and temperature and that the chemical reactions between the functional groups present on the sorbent and the metal ions are the rate-controlling step throughout the sorption process [40–42].

Adsorption Isotherm Models

To determine the behavior of Pb^{2+} ions on the surface of the adsorbent material during the adsorption process, the experimental data obtained was processed according to the Langmuir, Freundlich and Sips equilibrium isotherms, which describe well the adsorption processes. The adsorption isotherms of Pb^{2+} on the magnetic nanocomposite MNPs35@SiO_2 are shown in Figure 11, and the resulting parameters are shown in Table 8.

Table 8. Parameters of isotherm model for adsorption of Pb^{2+} onto magnetic nanocomposite.

Adsorption Isotherms									
Langmuir			Freundlich			Sips			
K_L (L·mg^{-1})	q_L (mg·g^{-1})	R^2	K_F (L·mg^{-1})	$1/n_F$	R^2	K_S (L·mg^{-1})	q_S (mg·g^{-1})	$1/n_S$	R^2
0.1449	17.1	0.9915	3.98	0.349	0.9290	0.056	17.6	0.15	0.9906
Experimental value			$q_{m,exp}$ (mg·g^{-1})				14.9		

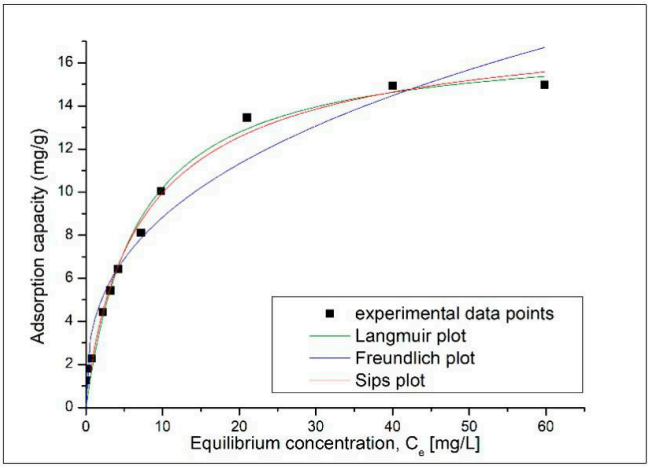

Figure 11. Adsorption isotherm of Pb^{2+} onto magnetic nanocomposite MNPs35@SiO_2.

According to the correlation coefficient R^2 the Langmuir isotherm describes best the adsorption process of Pb^{2+} on the MNPs35@SiO_2 nanocomposite. Moreover, q_L = 17.1 mg g^{-1}, is much closer to the experimental value, i.e., q_m, exp = 14.9 mg g^{-1}. According to the literature, the fact that the adsorption process is better modelled according to the Langmuir model shows that the adsorption process is positively influenced by the increase in the concentration of metal ions [14] and that the adsorption process of Pb^{2+} ions on the adsorbent occurs only in a monolayer, all surface sites are energetically identical housing a single Pb^{2+} ion, and the ability of a Pb^{2+} ion to adsorb on the surface is independent of occupying adjacent sites [43]. At the same time, the adsorption mechanism is controlled by chemosorption processes as a result of strong chelation between Pb^{2+} ions and OH^- groups and/or free electron pairs present on the surface of the adsorbent material [44]. By following the value of the coefficient n_s <2, we can confirm that the adsorption process is likely to occur by moving the metal ions from the aqueous phase to the surface of the nanocomposite.

Adsorption Thermodynamics

Usually, adsorption processes are significantly influenced by temperature. Therefore, to investigate the feasibility and the physiochemical characteristics, the effect of temperature (in the range of 298–318 K) on the adsorption of Pb^{2+} ions on the magnetic nanocomposite adsorbent MNPs35@SiO_2 was followed. The thermodynamic parameters were calculated from the slope and the intercept, by using linear plot of lnK_d function of 1/T, presented in Figure 12. Thermodynamic parameters: Gibbs free energy (ΔG°), free enthalpy (ΔH°), free entropy (ΔS°) and regression coefficient R^2 values are listed in Table 7.

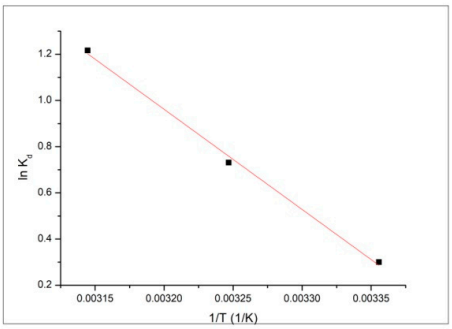

Figure 12. Adsorption isotherm of Pb^{2+} onto magnetic nanocomposite MNPs35@SiO_2.

The positive enthalpy value ΔH°, 36.1 kJ·mol^{-1}, showed that the adsorption process is endothermic in nature. When the adsorbent material is dispersed in solution, the intermolecular hydrogen from the water molecules interacts with oxygen-containing groups from the adsorbent surface, partially

converting them into hydrogen bonds. This tends to occupy the active sites of the adsorbent and consequently decrease the adsorption of Pb^{2+} ions [40]. The adsorption process in the solid–liquid system is a combination of two processes: (i) the desorption of the solvent (water) molecules adsorbed on the surface of the adsorbent, and (ii) the adsorption of the adsorbate species. In consequence, the energy required for the adsorption process is the energy consumed to displace the water molecules from the surface by the Pb^{2+} ions [41]. At the same time, the adsorption of Pb^{2+} ions involve electrostatic interactions and also possible complexation, that is consistent with the adsorption abilities at high temperature.

The value of the Gibbs free energy, ΔG°, -0.7 kJ·mol^{-1}, at 298 K, calculated from the experimental data, is negative, indicating that the adsorption of metal ions on the magnetic nanocomposite is a natural spontaneous process, and becomes more negative with the increase in temperature, -0.7, -1.9 and -3.1 kJ·mol^{-1} for 298 K, 308 K and 318 K, respectively, suggesting that the adsorption of Pb^{2+} ions increases with the temperature.

This can be attributed to effective surface growth contact between the adsorbent material and the metal ions. Also, this could be possible because the mobility of the Pb^{2+} ions in the solution increases with temperature and that the affinity of the metal ions on the magnetic nanocomposite is higher at high temperatures. The positive value of ΔS°, 123.4 J·(mol·K)$^{-1}$ reflects an increase in randomness during the process of Pb^{2+} ions adsorption on magnetic nanocomposite, and the existence of the affinity between the adsorbent and Pb^{2+} ions [41,42]. At the same time, the adsorption of Pb^{2+} ions involve electrostatic interactions and also possible complexation, which is consistent with the adsorption abilities at high temperature. The value of the Gibbs free energy, ΔG°, calculated from the experimental data, is negative, indicating that the adsorption of metal ions on the magnetic nanocomposite is a natural spontaneous process, and becomes more negative with the increase in temperature, suggesting that the adsorption of Pb^{2+} ions increases with the temperature. This can be attributed to effective surface growth contact between the adsorbent material and the metal ions. Also, this could be possible because the mobility of the Pb^{2+} ions in the solution increases with temperature and that the affinity of the metal ions on the magnetic nanocomposite is higher at high temperatures. The positive value of ΔS° reflects an increase in randomness during the process of Pb^{2+} ions adsorption on magnetic nanocomposite, and the existence of the affinity between the adsorbent and Pb^{2+} ions [45,46].

It is very difficult to compare the results with various data reported in the literature since the differences of lead adsorption capacities depend not only on the structure and morphology of the adsorbent such as surface area, porosity, presence of functional groups, but also on the adsorption process variables like pH, adsorbent dose, metal ion concentration, temperature, contact time etc. The complexity derives from the non-uniformity of the adsorption process variables employed and the different measuring units for adsorption capacity or parameters that were used to express the results. Roughly, functionalization of the silica shell is significant when the initial metal concentration is as low as 0.01–0.2 mg/mL [13,47,48] or when small quantities of adsorbent (0.4–1 mg/mL) [11,12,14–16] and reduced contact times (30 min) [12] should be used.

Finally, the selection of most suitable adsorbents should depend on a number of factors including cost-effectiveness, availability, and reusability. The results showed that our nanocomposite material exhibit Pb^{2+} adsorption properties comparable with some of the functionalized ones, an increase of the adsorption properties being obtained mainly for porous silica nanocomposites and for materials with hybrid coating which follows multilayer adsorption. Functionalization of the silica considerably reduces the contact time and the quantity of adsorbent used. However, the physico-chemical stability and economic issues regarding the adsorbent cost should be taken into account.

3.2.5. Desorption Experiments

Beside the adsorption capacity one important parameter characterizing the adsorbent materials to be used for practical applications is represented by the regenerative capacity of the material, which is translated into the possibility to reuse such materials. To be able to reuse an adsorbent material, it is

necessary for the metal ions to be easily desorbed from its surface and obviously in an amount large enough to be reusable. In this paper, the possibility of desorption of Pb^{2+} ions from the surface of magnetic MNPs35@SiO_2 nanocomposite was followed. The desorption process was performed with a good efficiency using 5% HCl and was 95.7%.

4. Conclusions

Three magnetic nanocomposite iron oxide-silica shell materials were synthesized containing a different mass percent of iron oxide nanoparticles of around 10 nm diameter. The morphology of the nanocomposites depended on the mass percentage of MNPs used in the synthesis. The sample with the highest surface and best magnetic properties was chosen to conduct Pb^{2+} adsorption studies from aqueous media (MNPs35@SiO_2).

MNPs35@SiO_2 presented a relatively high value of specific surface area 271.0 m^2 g^{-1}, total pore volume 1.0 cm^3 g^{-1} and pore diameter 24.9 nm. The saturation magnetization value obtained for the nanocomposite, 12.4 emu g^{-1}, indicated that the synthesized material has a good response to an external magnetic field, which is an important feature for the applicability as adsorbent for removing heavy metals from waste water. The maximum adsorption capacity, 14.9 mg·g^{-1}, is comparable with results obtained for similar nanocomposites reported in literature.

The adsorption mechanism of Pb^{2+} ions was established by kinetic, thermodynamic and equilibrium studies. The results indicated that the adsorption takes place at the surface of the material, being a spontaneous, endothermic process and physical bonds may be involved (hydrogen bonding or electrostatic attraction), but the process is mainly governed by chemisorption. Finally, for better process efficiency and ensuing widespread use, being affordable and with good stability, Pb^{2+} desorption studies were conducted, establishing that it may be reused with good efficiency.

Author Contributions: Conceptualization, A.-M.P. and E.I.S.; synthesis: R.N. and E.-M.P.; structural characterization: R.N.; nitrogen sorption: C.I.; SANS: A.L. and L.A.; XRD: R.L.; adsorption studies: M.C.; A.N.; writing—original draft preparation, A.-M.P. and E.I.S.; writing—review and editing, E.I.S. and O.C. All authors have read and agreed to the published version of the manuscript.

Funding: This research received no external funding.

Acknowledgments: The authors thank to Aurel Ercuta from West University of Timisoara, Romania for magnetic measurements and fruitful discussions. The authors thank to the Romanian Academy (Program 4) and the Inter-Academic Exchange Programs between Academy of Sciences of the Czech Republic and Romanian Academy and Hungarian Academy of Sciences and Romanian Academy. This work is dedicated to the memory of Assoc. Daniel Nižňanský (1963–2018) from Charles University of Prague and the Academy of Sciences of the Czech Republic.

Conflicts of Interest: The authors declare no conflict of interest. The funders had no role in the design of the study; in the collection, analyses, or interpretation of data; in the writing of the manuscript; or in the decision to publish the results.

References

1. Masindi, V.; Muedi, K.L. Chapter 7: Environmental Contamination by Heavy Metals. In *Heavy Metals*; Saleh, H.E.-D.M., Aglan, R.F., Eds.; Publisher IntechOpen: London, UK, 2018.
2. Fu, F.; Wang, Q. Removal of heavy metal ions from wastewaters: A review. *J. Environ. Manag.* **2011**, *92*, 407–418. [CrossRef] [PubMed]
3. Jawed, A.; Saxena, V.; Pandey, L.M. Engineered nanomaterials and their surface functionalization for the removal of heavy metals: A review. *J. Water. Process. Eng.* **2020**, *33*, 101009. [CrossRef]
4. Zhou, Q.; Li, J.; Wang, M.; Zhao, D. Iron-based magnetic nanomaterials and their environmental applications. *Crit. Rev. Environ. Sci. Technol.* **2016**, *46*, 783–826. [CrossRef]
5. Parkinson, G.S. Iron oxide surfaces. *Surf. Sci. Rep.* **2016**, *71*, 272–365. [CrossRef]
6. Roca, A.G.; Gutiérrez, L.; Gavilán, H.; Brollo, M.E.F.; Veintemillas-Verdaguer, S.; del Puerto Morales, M. Design strategies for shape-controlled magnetic iron oxide nanoparticles. *Adv. Drug Deliv. Rev.* **2019**, *138*, 68–104. [CrossRef]

7. Bhateria, R.; Singh, R. A review on nanotechnological application of magnetic iron oxides for heavy metal removal. *J. Water Process Eng.* **2019**, *31*, 100845. [CrossRef]
8. Jiang, F.; Fua, Y.; Zhu, Y.; Tang, Z.; Sheng, P. Fabrication of iron oxide/silica core–shell nanoparticles and their magnetic characteristics. *J. Alloys Comp.* **2012**, *543*, 43–48. [CrossRef]
9. Manyangadze, M.; Chikuruwo, N.H.M.; Narsaiah, T.B.; Chakra, C.S.; Radhakumari, M.; Danha, G. Enhancing adsorption capacity of nano-adsorbents via surface modification: A review. *S. Afr. J. Chem. Eng.* **2020**, *31*, 25–32. [CrossRef]
10. Abdullah, N.H.; Shameli, K.; Abdullah, E.C.; Abdullah, L.C. Solid matrices for fabrication of magnetic iron oxide nanocomposites: Synthesis, properties, and application for the adsorption of heavy metal ions and dyes. *Compos. Part-B* **2019**, *162*, 538–568. [CrossRef]
11. Aiello, D.; Talarico, A.M.; Teocoli, F.; Szerb, E.I.; Aiello, I.; Testa, F.; Ghedini, M. Self-incorporation of a luminescent neutral iridium(III) complex in different mesoporous micelle-templated silica. *New J. Chem.* **2011**, *35*, 141–148. [CrossRef]
12. Ahmad, N.; Sereshti, H.; Mousazadeh, M.; Nodeh, H.R.; Kamboh, M.A.; Mohamad, S. New magnetic silica-based hybrid organic-inorganic nanocomposite for the removal of lead(II) and nickel(II) ions from aqueous solutions. *Mater. Chem. Phys.* **2019**, *226*, 73–81. [CrossRef]
13. Mahmoud, M.E.; Abdelwah, M.S.; Fathallah, E.M. Design of novel nano-sorbents based on nano-magnetic iron oxide–bound-nano-silicon oxide–immobilized-triethylenetetramine for implementation in water treatment of heavy metals. *Chem. Eng. J.* **2013**, *223*, 318–327. [CrossRef]
14. Shi, H.; Yang, J.; Zhu, L.; Yang, Y.; Yuan, H.; Yang, Y.; Liu, X. Removal of Pb^{2+}, Hg^{2+}, and Cu^{2+} by Chain-Like Fe_3O_4@SiO_2@Chitosan Magnetic Nanoparticles. *J. Nanosci. Nanotechnol.* **2016**, *16*, 1871–1882. [CrossRef] [PubMed]
15. Wang, J.; Zheng, S.; Shao, Y.; Liu, J.; Xu, Z.; Zhu, D. Amino-functionalized Fe_3O_4@SiO_2 core–shell magnetic nanomaterial as a novel adsorbent for aqueous heavy metals removal. *J. Colloid Interf. Sci.* **2010**, *349*, 293–299. [CrossRef] [PubMed]
16. Culita, D.C.; Simonescu, C.M.; Patescu, R.-E.; Dragne, M.; Stanica, N.; Oprea, O. *o*-Vanillin functionalized mesoporous silica—Coated magnetite nanoparticles for efficient removal of Pb(II) from water. *J. Solid State Chem.* **2016**, *238*, 311–320. [CrossRef]
17. Tian, Q.; Wang, X.; Mao, F.F.; Guo, X.Y. Absorption performance of DMSA modified Fe_3O_4@SiO_2 core/shell magnetic nanocomposite for Pb^{2+} removal. *J. Cent. South Univ.* **2018**, *25*, 709–718. [CrossRef]
18. Suleiman, J.S.; Hu, B.; Peng, H.; Huang, C. Separation/preconcentration of trace amounts of Cr, Cu and Pb in environmental samples by magnetic solid-phase extraction with Bismuthiol-II-immobilized magnetic nanoparticles and their determination by ICP-OES. *Talanta* **2009**, *77*, 1579–1583. [CrossRef]
19. Fang, X.; Zhao, X.; Fang, W.; Chen, C.; Zheng, N. Self-templating synthesis of hollow mesoporous silica and their applications in catalysis and drug delivery. *Nanoscale* **2013**, *5*, 2205–2218. [CrossRef] [PubMed]
20. Chen, D.; Li, L.; Tang, F.; Qi, S. Facile and Scalable Synthesis of Tailored Silica "Nanorattle" Structures. *Adv. Mater.* **2009**, *21*, 3804–3807. [CrossRef]
21. Hu, H.; Wang, Z.; Pan, L. Synthesis of monodisperse Fe_3O_4@silica core–shell microspheres and their application for removal of heavy metal ions from water. *J. Alloys Compd.* **2010**, *492*, 656–661. [CrossRef]
22. Ercuta, A. Sensitive AC Hysteresisgraph of extended driving field capability. *IEEE Trans. Instrum. Meas.* **2020**, *69*, 1643–1651. [CrossRef]
23. Becauge, G. Small-Angle Scattering from Polymeric Mass Fractals of Arbitrary Mass-Fractal Dimension. *J. Appl. Cryst.* **1996**, *29*, 134–146. [CrossRef]
24. Nicola, R.; Costişor, O.; Ianăşi, C.; Lazau, R.; Sacarescu, L.; Niznansky, D.; Ercuta, A.; Putz, A.-M.; Savii, C. Fractal Surface Maghemite Nanoparticles Prepared by Co-precipitation: The Influence of Iron Concentration and Base Nature. *Studia UBB Chemia LXIII* **2018**, *4*, 15–29. [CrossRef]
25. Hui, C.; Shen, C.; Tian, J.; Bao, L.; Ding, H.; Li, C.; Tian, Y.; Shia, X.; Gao, H.-J. Core-shell Fe_3O_4@SiO_2 nanoparticles synthesized with well-dispersed hydrophilic Fe_3O_4 seeds. *Nanoscale* **2011**, *3*, 701–705. [CrossRef]
26. Ahangaran, F.; Hassanzadeh, A.; Nouri, S. Surface modification of Fe_3O_4@SiO_2 microsphere by silane coupling agent. *Int. Nano Lett.* **2013**, *3*, 23–28. [CrossRef]
27. Ianasi, C.; Piciorus, M.; Nicola, R.; Ciopec, M.; Negrea, A.; Niznansky, D.; Len, A.; Almasy, L.; Putz, A.-M. Removal of cadmium from aqueous solutions using inorganic porous nanocomposites. *Korean J. Chem. Eng.* **2019**, *36*, 688–700.

28. Fagadar-Cosma, E.; Dudás, Z.; Birdeanu, M.; Almásy, L. Hybrid organic-silica nanomaterials based on novel A_3B mixed substituted porphyrin. *Mater. Chem. Phys.* **2014**, *148*, 143–152. [CrossRef]
29. Putz, A.-M.; Len, A.; Ianasi, C.; Savii, C.; Almásy, L. Ultrasonic preparation of mesoporous silica using pyridinium ionic liquid. *Korean J. Chem. Eng.* **2016**, *33*, 749–754. [CrossRef]
30. Gubanova, N.N.; Baranchikov, A.Y.; Kopitsa, G.P.; Almásy, L.; Angelov, B.; Yapryntsev, A.D.; Rosta, L.; Ivanov, V.K. Combined SANS and SAXS study of the action of ultrasound on the structure of amorphous zirconia gels. *Ultrason. Sonochem.* **2015**, *24*, 230–237. [CrossRef]
31. Dudás, Z.; Fagadar-Cosma, E.; Len, A.; Románszki, L.; Almásy, L.; Vlad-Oros, B.; Dascălu, D.; Krajnc, A.; Kriechbaum, M.; Kuncser, A. Improved Optical and Morphological Properties of Vinyl-Substituted Hybrid Silica Materials Incorporating a Zn-Metalloporphyrin. *Materials* **2018**, *11*, 565. [CrossRef]
32. Thommes, M.; Kaneko, K.; Neimark, A.V.; Olivier, J.P.; Rodriguez-Reinoso, F.; Rouquerol, J.; Sing, K.S.W. Physisorption of gases, with special reference to the evaluation of surface area and pore size distribution (IUPAC Technical Report). *Pure Appl. Chem.* **2015**, *87*, 1051–1069. [CrossRef]
33. Negrea, A.; Lupa, L.; Ciopec, M.; Lazau, R.; Muntean, C.; Negrea, P. Adsorption of As(III) ions onto iron-containing waste sludge. *Ads. Sci. Technol.* **2010**, *28*, 467–480. [CrossRef]
34. Ho, Y.S. Effect of pH on lead removal from water using tree fern as the sorbent. *Bioresour. Technol.* **2005**, *96*, 1292–1296. [CrossRef] [PubMed]
35. Esposito, A.; Pagnanelli, F.; Vegliò, F. pH-related equilibria models for biosorption in single metal systems. *Chem. Eng. Sci.* **2002**, *57*, 307–313. [CrossRef]
36. Aksu, Z.; İsoğlu, I.A. Removal of copper (II) ions from aqueous solution by biosorption onto agricultural waste sugar beet pulp. *Process. Biochem.* **2005**, *40*, 3031–3044.
37. Sharma, R.K.; Puri, A.; Monga, Y.; Adholeya, A. Acetoacetanilide-functionalized Fe_3O_4 nanoparticles for selective and cyclic removal of Pb^{2+} ions from different charged wastewaters. *J. Mater. Chem. A* **2014**, *2*, 12888–12898. [CrossRef]
38. Bhalara, P.D.; Punetha, D.; Balasubramanian, K. A review of potential remediation techniques for uranium (VI) ion retrieval from contaminated aqueous environment. *J. Env. Chem. Eng.* **2014**, *2*, 1621–1634. [CrossRef]
39. Ho, Y.S. Review of second-order models for adsorption systems. *J. Hazard. Mater.* **2006**, *136*, 681–689. [CrossRef]
40. Plaza, C.J.; Viera, M.; Donati, E.; Guibal, E. Zinc and cadmium removal by biosorption on Undaria pinnatifida in batch and continuous processes. *J. Environ. Manag.* **2013**, *129*, 423–434. [CrossRef]
41. Ramos, S.N.C.; Xavier, A.L.P.; Teodoro, F.S.; Elias, M.M.C.; Gonçalves, F.J.; Gil, L.F.; de Freita, R.P.; Gurgel, L.V.A. Modeling mono- and multi-component adsorption of cobalt(II), copper(II) and nickel(II), metal ions from aqueous solution onto a new carboxylated sugarcane bagasse. Part I: Batch adsorption study. *Ind. Crops Prod* **2015**, *74*, 357–371. [CrossRef]
42. Sun, L.; Wang, J.; Wu, J.; Wang, T.; Du, Y.; Li, Y.; Li, H. Constructing nanostructured silicates on diatomite for Pb(II) and Cd(II) removal. *J. Mater. Sci.* **2019**, *54*, 6882–6894. [CrossRef]
43. Kucuker, M.A.; Wieczorek, N.; Kuchta, K.; Copty, N.K. Biosorption of neodymium on Chlorella vulgaris in aqueous solution obtained from hard disk drive magnets. *PLoS ONE* **2017**, *12*, e0175255. [CrossRef]
44. Sitko, R.; Turek, E.; Zawisza, B.; Malicka, E.; Talik, E.; Heimann, J.; Gagor, A.; Feist, B.; Wrzalik, R. Adsorption of divalent metal ions from aqueous solutions using graphene oxide. *Dalton Trans.* **2013**, *42*, 5682–5689. [CrossRef] [PubMed]
45. Saha, P.; Chowdhury, S. Insight into adsorption thermodynamics. In *Thermodynamics*; Tadashi, M., Ed.; InTech: London, UK, 2011; pp. 349–364.
46. Liu, Z.; Shen, Q.; Zhang, Q.; Bian, L.; Liu, Y.; Yuan, B.; Pan, X.; Jiang, F. The removal of lead ions of the aqueous solution by calcite with cotton morphology. *J. Mater. Sci.* **2014**, *49*, 5334–5344. [CrossRef]
47. Sinha, A.; Jana, R.N. Functional, mesoporous, superparamagnetic colloidal sorbents for efficient removal of toxic metals. *Chem. Comm* **2012**, *48*, 9272–9274. [CrossRef]
48. Zhang, M.; Zhang, Z.; Liu, Y.; Yang, X.; Luo, L.; Chen, J.; Yao, S. Preparation of core-shell magnetic ion-imprinted polymer for selective extraction of Pb(II) from environmental samples. *Chem. Eng. J.* **2011**, *178*, 443–450. [CrossRef]

© 2020 by the authors. Licensee MDPI, Basel, Switzerland. This article is an open access article distributed under the terms and conditions of the Creative Commons Attribution (CC BY) license (http://creativecommons.org/licenses/by/4.0/).